Research Article

ADVANCED PHOTONICS

Electro-optic tuning of a single-frequency ultranarrow linewidth microdisk laser

Jintian Lin,[a,b,†] Saeed Farajollahi,[c,†] Zhiwei Fang,[d,†] Ni Yao,[e,f] Renhong Gao,[a,b] Jianglin Guan,[d,g] Li Deng,[d,g] Tao Lu,[c,*] Min Wang,[d,g] Haisu Zhang,[d,g] Wei Fang,[f,h,*] Lingling Qiao,[a,b] and Ya Cheng[a,b,d,g,i,j,k,*]

[a]Chinese Academy of Sciences (CAS), Shanghai Institute of Optics and Fine Mechanics (SIOM), State Key Laboratory of High Field Laser Physics and CAS Center for Excellence in Ultra-Intense Laser Science, Shanghai, China
[b]University of Chinese Academy of Sciences, Center of Materials Science and Optoelectronics Engineering, Beijing, China
[c]University of Victoria, Department of Electrical and Computer Engineering, Victoria, British Columbia, Canada
[d]East China Normal University, School of Physics and Electronic Science, XXL—The Extreme Optoelectromechanics Laboratory, Shanghai, China
[e]Research Center for Intelligent Sensing, Zhejiang Lab, Hangzhou, China
[f]Zhejiang University, College of Optical Science and Engineering, The Interdisciplinary Center for Quantum Information, State Key Laboratory of Modern Optical Instrumentation, Hangzhou, China
[g]East China Normal University, State Key Laboratory of Precision Spectroscopy, Shanghai, China
[h]Jiaxing Institute of Zhejiang University, Intelligent Optics & Photonics Research Center, Jiaxing, China
[i]Shanxi University, Collaborative Innovation Center of Extreme Optics, Taiyuan, China
[j]Shandong Normal University, Collaborative Innovation Center of Light Manipulations and Applications, Jinan, China
[k]Shanghai Research Center for Quantum Sciences, Shanghai, China

Abstract. Single-frequency ultranarrow linewidth on-chip microlasers with a fast wavelength tunability play a game-changing role in a broad spectrum of applications ranging from coherent communication, light detection and ranging, to metrology and sensing. Design and fabrication of such light sources remain a challenge due to the difficulties in making a laser cavity that has an ultrahigh optical quality (Q) factor and supports only a single lasing frequency simultaneously. Here, we demonstrate a unique single-frequency ultranarrow linewidth lasing mechanism on an erbium ion-doped lithium niobate (LN) microdisk through simultaneous excitation of high-Q polygon modes at both pump and laser wavelengths. As the polygon modes are sparse within the optical gain bandwidth compared with the whispering gallery mode counterpart, while their Q factors (above 10 million) are even higher due to the significantly reduced scattering on their propagation paths, single-frequency lasing with a linewidth as narrow as 322 Hz is observed. The measured linewidth is three orders of magnitude narrower than the previous record in on-chip LN microlasers. Finally, enabled by the strong linear electro-optic effect of LN, real-time electro-optical tuning of the microlaser with a high tuning efficiency of ~50 pm/100 V is demonstrated.

Keywords: lasers; lithium niobate; microcavities; integrated optics.

Received Nov. 23, 2021; revised manuscript received Feb. 24, 2022; accepted for publication Mar. 30, 2022; published online May 3, 2022.

[DOI: 10.1117/1.AP.4.3.036001]

1 Introduction

Broad transparency window and high piezoelectric, acousto-optic, second-order nonlinear, and electro-optic (EO) coefficients characterize crystalline lithium niobate (LN) as the "silicon in photonics."[1–7] Recent breakthroughs in the nanofabrication technology on thin-film LN platforms[4] gave birth to a variety of integrated photonic devices such as high-performance EO modulators,[8,9] broadband optical frequency combs,[10–12] and high efficiency frequency converters.[13–15] To build a monolithic integrated photonic system on an LN chip, the capacity of microlaser

*Address all correspondence to Tao Lu, taolu@ece.uvic.ca; Wei Fang, wfang08@zju.edu.cn; Ya Cheng, ya.cheng@siom.ac.cn.

†These authors contributed equally to the work.

fabrication on this platform is essential. The high EO coefficient of LN ensures that such lasers outperform all other on-chip counterparts in broad range and real-time wavelength tunability. However, similar to silicon, LN itself does not provide optical gain for lasing. Therefore, to functionalize LN, doping of the gain medium is necessary. In particular, to make lasers operating at widely needed telecom wavelengths, the erbium ion (Er^{3+}) is a favorable choice of dopant.[16–22] More importantly, to enable many applications and outperform silicon counterparts, such lasers should operate at a single frequency with an ultranarrow linewidth and fast wavelength tunability.[23–27] According to the Schawlow–Townes theory, the laser fundamental linewidth is quadratic inversely proportional to the undoped cavity Q factor.[28–30] Therefore, increasing the Q factor will quadratically reduce the linewidth of a microlaser. The highest Q factors demonstrated to date are those of whispering gallery mode (WGM) microcavities where light confinement is achieved by continuous total internal reflection at the smooth resonator periphery.[31] However, the dense WGMs within the optical gain bandwidth would easily lead to multifrequency lasing in a microcavity. To reduce the number of modes, attempts have been made to reduce the microcavity size,[23] which inevitably increases the radiation loss and decreases the mode volume, leading to a reduction of both the Q factor and optical gain in the microcavity. Consequently, the pump threshold increases while the laser power remains low.

The polygon-shaped modes in large LN microdisks have demonstrated high Q factors due to reduced scattering losses on their propagation paths.[32] In this work, by exciting polygon modes and avoiding the dense WGMs, we demonstrated single-frequency lasing in large Er^{3+}-doped LN microdisks with an ultranarrow linewidth. EO tuning of the laser wavelength was realized with a high linear tuning efficiency of 50 pm/100 V.

2 Construction of the Microlaser

2.1 Active Microdisk Fabrication

The fabrication process of the microdisk begins from the preparation of an Er^{3+}-doped Z-cut LN thin-film wafer by ion slicing. The doping concentration of Er^{3+} is 1% (mole fraction). The fabrication flow of the microdisk resonators mainly consists of four steps. First, a chromium (Cr) thin layer was coated on the LN thin-film wafer and then patterned into microdisks using femtosecond laser micromachining. The removal of the Cr thin film with a high spatial resolution was achieved by femtosecond laser ablation. Second, the microdisk pattern was transferred from the Cr layer to the LN thin film via chemo-mechanical polishing. Third, the microelectrodes were fabricated on the Cr layer again using the space-selective femtosecond laser ablation. Finally, the silica layer underneath the LN disk was partially undercut to form the supporting pedestals for supporting the LN thin-film microdisks. The details of the fabrication can be found in Refs. 17 and 33. An optical micrograph of the fabricated microdisk integrated with electrodes is shown in the inset of Fig. 1 (bottom right). The distance between the microelectrodes is 35 μm. The zoom-in scanning electron microscope (SEM) image of the fabricated microcavity without microelectrodes is also shown in the inset of Fig. 1 (bottom middle), which consists of an Er^{3+}-doped LN microdisk with a thickness of 700 nm and a diameter ~29.8 μm, indicating an ultrasmooth surface. The microdisk is supported by a thin silica pedestal (with a diameter of ~8 μm) on the LN substrate. The principal dielectric axes x, y of LN are illustrated in the inset of Fig. 1.

2.2 Experimental Setup

The experimental setup is illustrated in Fig. 1. A narrow-linewidth tunable diode laser (Model: TLB-6719, New Focus, Inc.)

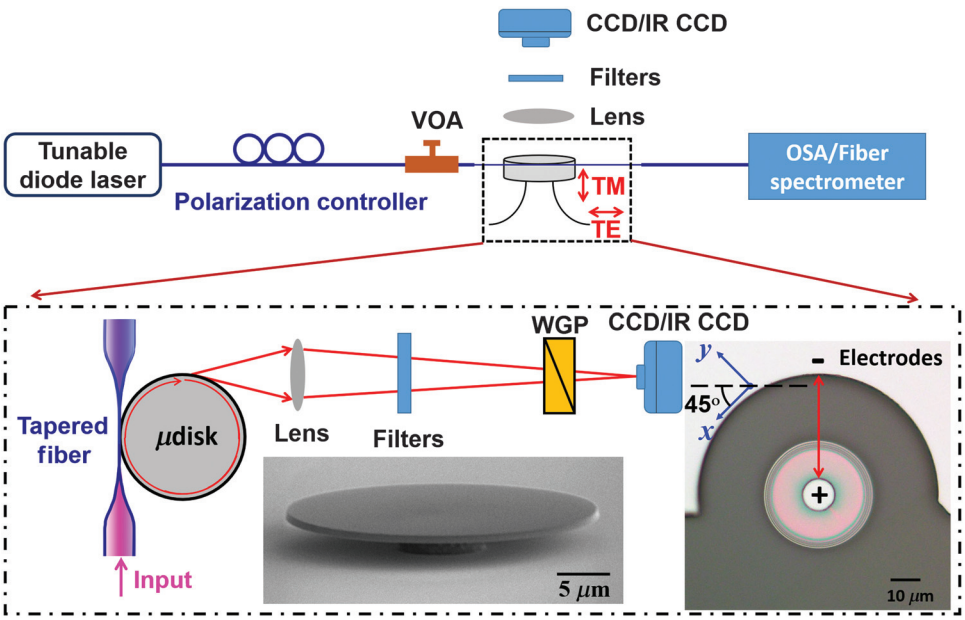

Fig. 1 The experimental setup for lasing and polarization measurement. A variable optical attenuator (VOA) was used to tune the input power into the Z-cut microdisk. TM and TE represent transverse magnetic and transverse electric polarization states, respectively. Inset: SEM image of the microdisk (without electrodes) and optical micrograph of the microdisk integrated with Cr electrodes.

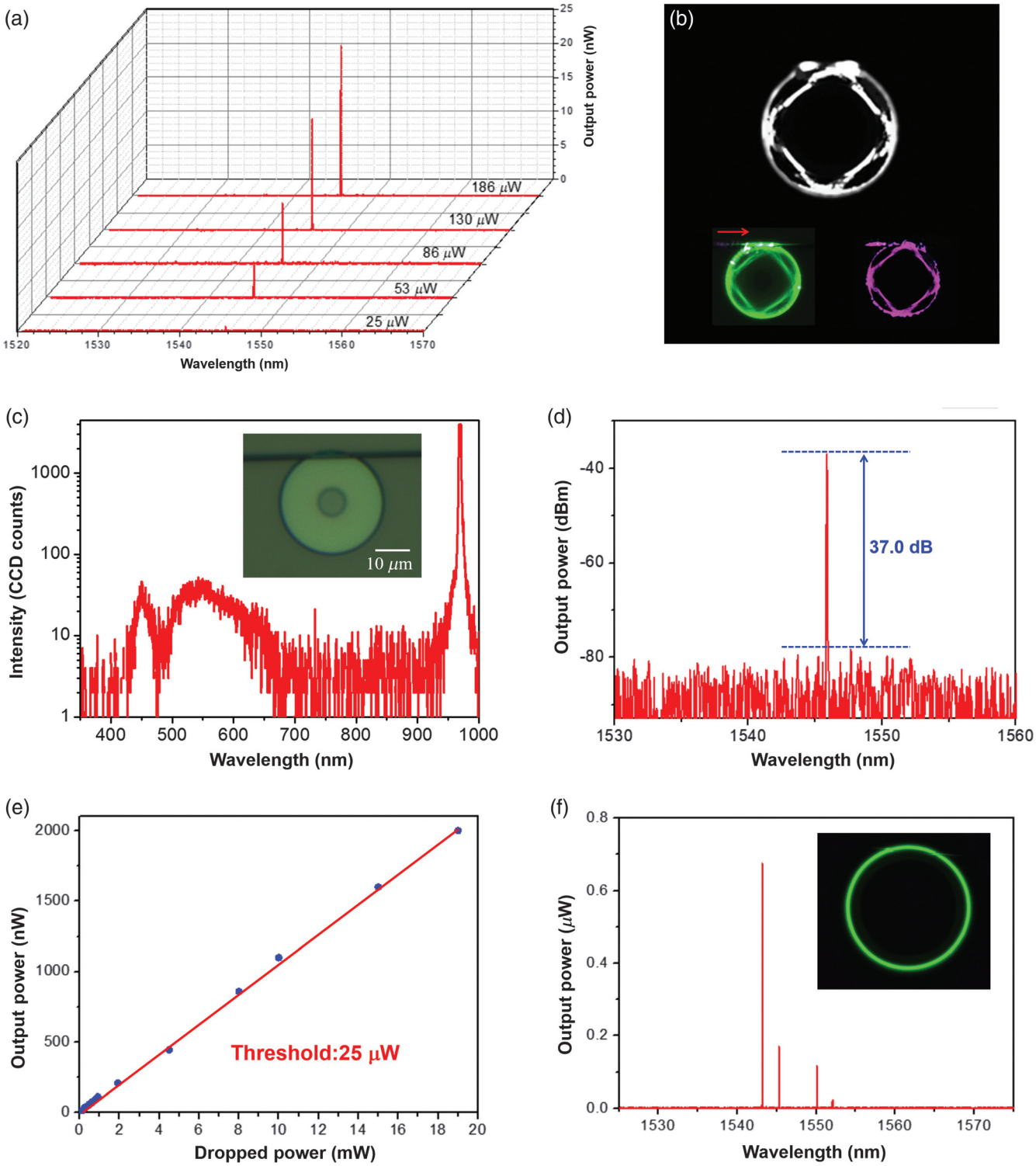

Fig. 2 (a) Spectra of the microlaser output powers at different pump power levels. (b) The optical micrograph of the square lasing mode at 1546-nm wavelength. Inset: the optical micrographs of the square modes of the upconversion fluorescence around the 550-nm wavelength (left) and the pump light (right). (c) Spectrum of the upconversion fluorescence and the pump light. Inset: optical micrograph of the tapered fiber coupled with the microdisk. (d) Spectrum of lasing. (e) Laser output power versus pump power dropped to the cavity shows a pump threshold of 25 μW. (f) Spectrum of multiple-mode lasing when pumping with a WGM at 971.5-nm wavelength. Inset: the optical micrograph of the upconversion fluorescence, showing a circular pattern along the disk periphery.

was used as the pump light source, and the pump laser wavelength was tuned to be resonant with a specific transverse electric (TE) polarized cavity mode around 968 nm. The laser was coupled to the microdisk via a tapered fiber with a waist size of 2 μm. The position between the tapered fiber and the microdisk was adjusted by a three-dimensional (3D) piezo stage with a 20-nm resolution. An optical imaging system consisting of a microscope objective lens with a numerical aperture (NA) of 0.42, long-pass filters (Thorlabs, Inc., Model: FELH1100), and an infrared (IR) charge-coupled device (CCD) was used to monitor the coupling system from the top and capture the intensity profile of the lasing modes around 1550-nm wavelength. To capture the intensity profiles of the pump mode and upconversion fluorescence signal in the microdisk, a visible CCD and a set of long-pass filters and short-pass filters (Thorlabs, Inc., Model: FEL800 and FES800) were used to take the place of the IR CCD and long-pass filters in the optical micrograph system for blocking the upconversion fluorescence, and combination of the pump light and the lasing signal, respectively. The generated emission from the microdisk was coupled out by the same tapered fiber and sent into either an optical spectrum analyzer (OSA for short, YOKOGAWA, Inc., Model AQ6370D, detection range: 600 to 1700 nm) or a fiber spectrometer [Ocean Optics, Inc., Model USB2000+ (VIS-NIR), detection range: 350 to 1000 nm] for spectral analysis. Meanwhile, the polarization states of the pump and lasing modes were checked via a precalibrated wire grating polarizer (WGP) by collecting the signals scattered from the edge of the microdisk. The resolutions of the OSA and the spectrometer were set as 0.01 and 1.5 nm, respectively.

2.3 Polygon Mode Formation

When the relative position between the tapered fiber and the center of the microdisk was adjusted to 13.37 μm [inset in Fig. 2(c)], the single-mode laser peaking at 1546-nm wavelength was observed in TE polarization, as shown in Fig. 2(a). The IR CCD captured the top view of the lasing mode in Fig. 2(b), which displays a square pattern in the microdisk. The large overlap between the lasing mode pattern and those of the pump mode at 968 nm and the upconversion fluorescence at ~550-nm wavelengths [shown in Fig. 2(b)], ensures that conventional high-density WGMs circulating around the circumference of the disk cannot be efficiently excited. The relatively large free spectral range (FSR) of 11.5 nm facilitates single-mode lasing within the gain bandwidth of Er^{3+}. Figure 2(d) confirms that the laser exhibits a side mode suppression ratio of 37.0 dB. The output power of the laser signal as a function of the pump power is plotted in Fig. 2(e), indicating a lasing threshold of merely ~25 μW. The maximum output power of the microlaser was measured as 2 μW (i.e., −27.0 dBm) when the dropped pump power was 20 mW. For comparison, we also pumped the microdisk to exhibit a conventional WGM at the pump laser wavelength of 971.5 nm, giving rise to the multiple-mode lasing shown in Fig. 2(f).

2.4 Mode Structure Measurements

In principle, WGMs feature ultrahigh Q factors based on the nature of total internal reflection. In reality, however, these modes suffer from the inevitable surface roughness introduced during fabrication, as their optical pathways overlap with the

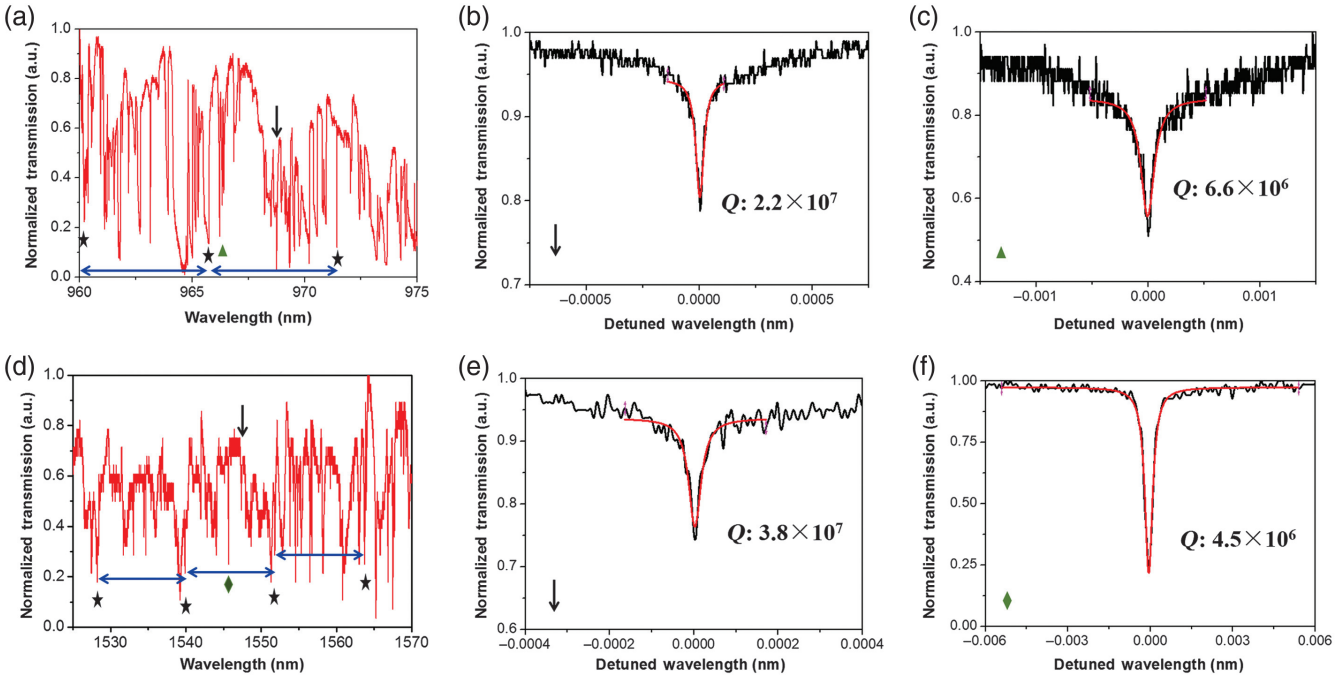

Fig. 3 Transmission spectra of the tapered fiber coupled with the microdisk. (a) Transmission spectrum around the pump wavelength, where each blue line segment with two arrows indicates an FSR. (b) The Q factor of the pump mode. (c) The measured highest Q factor of the conventional WGM [indicated with a green triangle in (a)] within one FSR. (d) Spectrum around the lasing wavelength. (e) The Q factor of the lasing mode. (f) The measured highest Q factor of the conventional WGM [indicated with a green rhombus in (d)] within one FSR.

periphery of the cavity. The polygon modes have their main propagation paths away from the boundary yet preserve the total internal reflection condition at the bouncing points. Thus, polygon modes can have competitively high Q factors over those of WGMs. This was proved experimentally based on an undoped microdisk that had the same geometry as the microlaser. Figures 3(a) and 3(d) show the transmission spectra around 968 and 1546 nm when two tunable diode lasers (Model: TLB-6719 & 6728, New Focus, Inc.) with an output power of 5 μW were used to investigate the modes at the pump and lasing wavelength range. The tapered fiber was placed at the same location as the microlaser experiment, so that polygon modes were excited in both wavelength regions. The loaded Q factors of polygon modes at 968- and 1546-nm wavelength [Figs. 3(b) and 3(e)] were both measured to be above 10^7, about one order of magnitude higher than that of conventional WGMs in the vicinity [Figs. 3(c) and 3(f)].

2.5 Linewidth Characterization

With such a high Q factor, a laser based on the polygon mode can have an ultranarrow linewidth based on the relationship between the laser linewidth and the Q factor of an undoped cavity.[32] As shown in Fig. 4(a), we measured the linewidth by heterodyning two independently pumped single-mode microlasers.[34] Since the two microdisks have the same diameter, a relative lasing frequency difference of ~1 MHz can be achieved by adjusting the pump powers.[16–19,22] The two laser signals were photo-mixed with a 3-dB optical directional coupler and converted to electrical signals with a balanced photodetector for spectral analysis in the radio frequency (RF) domain, as illustrated in Fig. 4(a). Here, a polarization controller was used at the output of one of the microlasers to ensure the two laser signals were of the same polarization state when photo-mixing. The Lorentzian-shaped power spectrum of the beat note signal was captured by a real-time spectrum analyzer (RSA for short, Tektronix RSA5126B) with a resolution bandwidth of ~1 Hz. Figure 4(b) shows the RF spectrum around 1 MHz when the output powers of both microlasers were ~2 μW. The full width at half maximum of the detected signal was measured as 643 Hz. Accordingly, the linewidth of the microlaser was 322 Hz, assuming that the microdisks were identical. The power spectral density of the frequency noise was also recorded by the spectrum analyzer in the phase noise analysis mode, as shown in

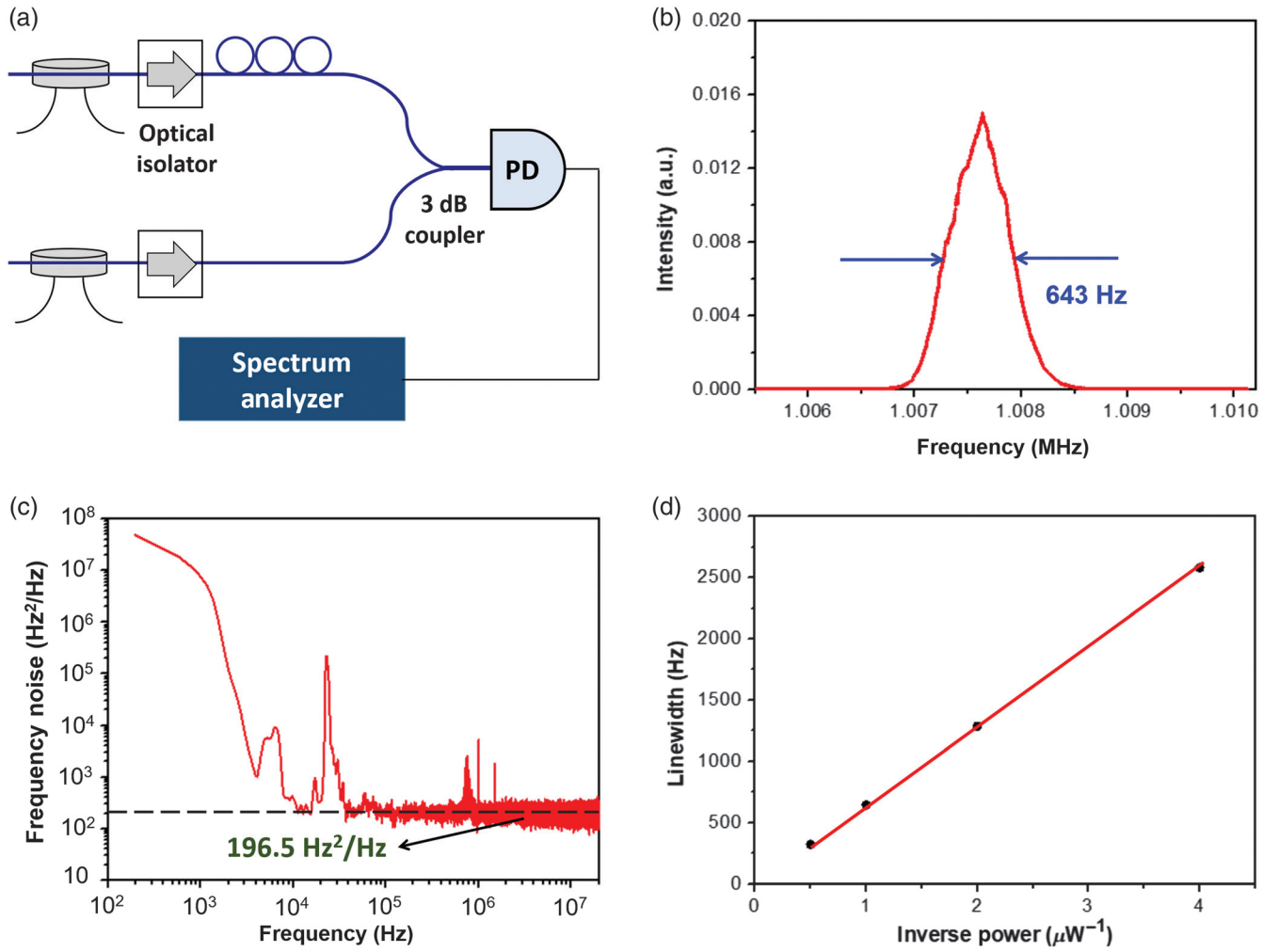

Fig. 4 Linewidth measurement. (a) The experimental setup. (b) The spectrum of the detected beating signal for an output power of 2 μW. (c) The measured frequency noise. (d) The linewidth is a function of the output power of the microlaser.

Fig. 4(c). At the high-frequency range (>0.5 MHz), the frequency noise is almost flat around 196.5 Hz^2/Hz, indicating a linewidth of 309 Hz, which is consistent with the result shown in Fig. 4(b). The linewidth of the microlaser as a function of the output power was further characterized. The inverse linear dependence of the linewidth versus output power agrees well with the Schawlow–Townes formula,[28–30] suggesting our microlaser linewidth is quantum noise limited. The measured linewidth is three orders of magnitude narrower than the previous record in on-chip LN microlasers.[16–22] In addition, the tuning of the microlaser as a function of the pump power in the MHz range can be resolved from the beat note signal captured by the RSA, which has been provided in the Supplementary Material. Here, the tuning efficiency agrees well with the results measured by the OSA.

2.6 Real-Time Wavelength Tuning

For the sake of application, the ability of wavelength tuning is usually required, especially for lasers with an ultranarrow linewidth. The wavelength of an LN microlaser can be tuned via temperature or pump power control.[16–19,22] The pump power tuning based on the combined significant photorefractive and thermo-optic effect is a spontaneous yet limited way.[22,35,36] As shown in Figs. 5(a) and 5(b), when the pump power dropped to the cavity increased from 1.92 to 20.00 mW, the laser wavelength shifted from 1545.633 to 1545.866 nm, corresponding to a wavelength tuning rate of 12.3 pm/mW (i.e., 1.54 MHz/μW). To achieve a fast wavelength tuning, the EO-based mechanism is the more favorable way, enabled by the strong linear EO effect of LN.[4] To introduce a refractive index change in the microdisk via the EO effect, a bias was applied between the circular microelectrode on the microdisk and the plane electrode integrated into the LN-on-insulator (LNOI) surface using two metal probes. The microelectrode integrated on the microdisk possesses a radius of 5 μm, as shown in the inset of Fig. 1. The electric potential and the electric field distribution are plotted in Figs. 5(c) and 5(d), respectively. The electric field distributed in the microdisk is mainly oriented in the radial direction. When the applied voltage was 1 V, the electric field strength was $\sim 2.08 \times 10^4$ V/m in the mode volume. Here, the EO coefficient r_{22} (6.8 pm/V) was utilized, and the details of the electrode design can be found in the Supplementary Material.[37,38] Figures 5(e) and 5(f) show the EO performance of the microlaser. When the voltage was tuned from −300 to 300 V, the lasing wavelength was redshifted from 1545.716 to 1546.017 nm, indicating a high linear tuning efficiency of 50 pm/100 V, which roughly agrees with the theoretically calculated value of 80 pm/100 V.[37] To access the largest EO coefficient r_{33} (30.9 pm/V), an X-cut LNOI substrate and TE polarized modes should be utilized. External wires can be directly integrated on the chip using air-bridge wiring[37] in future work.

3 Numerical Modeling

The underlying physics behind the polygon modes can be further explained by performing a 2D finite element simulation using COMSOL. In our simulation, the extraordinary and ordinary refractive indices of LN used in the simulation are $n_e = 2.1622$ and $n_o = 2.2393$ for the pump wavelength and $n_e = 2.1361$ and $n_o = 2.2113$ for the laser wavelength.[39] To provide sufficient perturbation for polygon modes, a tapered fiber is placed on top of the disk and we use the effective index method to compute the effective refractive index of the fiber-disk overlap

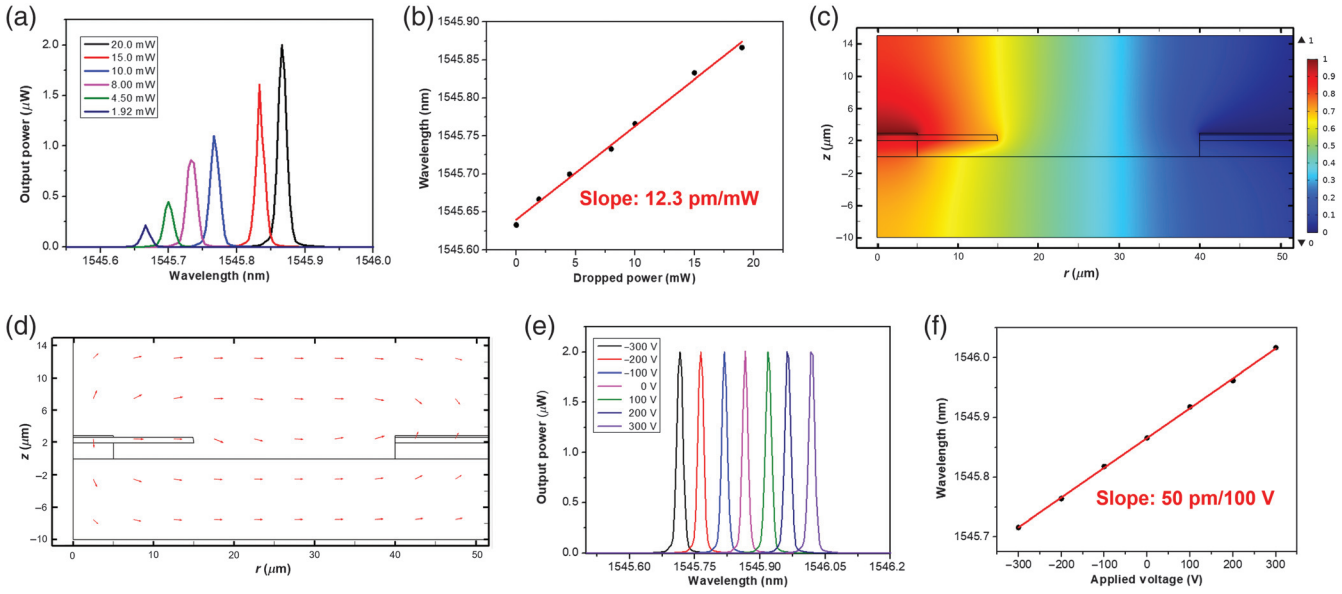

Fig. 5 (a) Lasing wavelength drift with different pump powers. (b) Lasing wavelength versus pump power. The linear fitting (red curve) shows a slope of 12.3 pm/mW. Distributions of (c) the scalar electric potential and (d) the vectorial electric field in the microdisk. The arrows denoting the vectorial electric field have a length proportional to the logarithm of the electric field magnitude. The material layers from top to bottom were Cr, LN, silica, and LN, respectively. (e) Lasing wavelength drift with the applied voltage. (f) Lasing wavelength versus applied voltage, showing a high tuning efficiency of 50 pm/100 V.

regime.[40,41] Figures 6(a) and 6(b) show the intensity profiles of the square mode and fundamental WGM at the pump wavelengths while Figs. 6(c), 6(f), and 6(i) display the square mode, fundamental, and high order WGMs, respectively. It is worth mentioning that within one FSR around each of the laser and pump wavelengths, multiple numbers of WGMs coexist but only the single square mode will appear due to the stringent requirement for polygon mode formation. We then compute the overlap factor Γ between different laser and pump modes defined by

$$\Gamma = \iiint \hat{I}_p \cdot \hat{I}_l \mathrm{d}v. \tag{1}$$

Here, $\hat{I}_p$ and $\hat{I}_l$ are normalized pump (I_p) and laser (I_l) intensities such that $\hat{I}_{p,l} = \frac{I_{p,l}}{\sqrt{\iiint I_{p,l}^2 \mathrm{d}v}}$ and $\iiint(\cdot)\mathrm{d}v$ is the volume integral over full space. The minimum pump threshold occurs when the laser and pump mode intensity overlap Γ is maximized, which can be found in the Supplementary Material.[42]

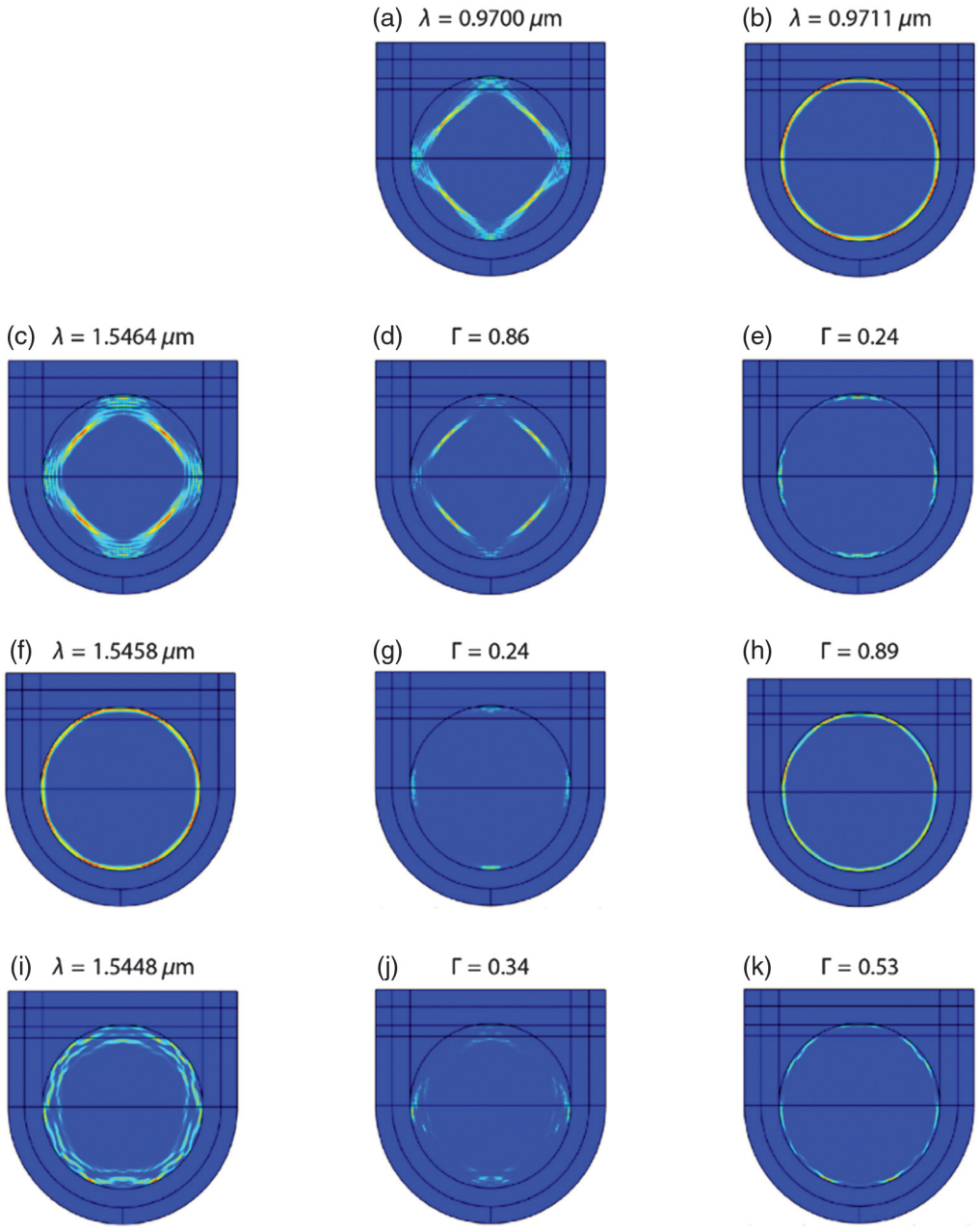

Fig. 6 The intensity distributions of (a) the square mode and (b) the fundamental WGM at the pump wavelengths. Left column: (c) the square mode, (f) the fundamental WGM, and (i) high order WGM at lasing wavelengths. (d)–(k) The intensity distributions of the integrand between each laser mode in the left column and either pump mode in the top row. Here, the larger overlap ($\Gamma = 0.53$) in (k) between the pump fundamental WGM and laser high-order WGM suggests that both the fundamental and high-order WGMs are likely to simultaneously lase, while in the case of being pumped by a square mode, the high-order WGM will not lase due to a lower overlap ($\Gamma = 0.34$).

The distributions of the integrand between different pump and laser modes are displayed in the rest of the subplots in Fig. 6. As shown, when the pump is in the square mode, its overlap factor with a square mode at the laser wavelength is $\Gamma = 0.86$ [Fig. 6(d)] while its overlap factor with the fundamental and high-order WGM can be as low as $\Gamma = 0.24$ [Fig. 6(g)] and $\Gamma = 0.34$ [Fig. 6(j)]. The significantly higher overlap coefficient ensures that only the square mode will have a sufficient optical gain for lasing. In addition, the FSR is larger than the gain bandwidth of Er^{3+}. Therefore, the square mode at neighboring FSRs will not be excited either due to lower gain. Consequently, single mode operation can be achieved when the polygon mode is formed at the pump wavelength. In contrast, when a regular WGM is formed by the pump, multiple WGMs within the gain bandwidth may lase simultaneously as the Γ of the laser and pump WGMs are close in value [e.g., the overlap between the pump fundamental WGM and high order laser mode can be as high as $\Gamma = 0.53$ (Fig. 6(k)]. Finally, it is also worth mentioning that the two-dimensional (2D) simulation will not allow the precise evaluation of the overall quality factor of the coupled cavity due to the unphysically large reflection incurred at the fiber-to-disk interfaces. The issue can be overcome with a full-wave 3D mode match method, which will be applied in future research.[40,41] Nevertheless, the 2D simulation results capture the essence of the polygon mode microlaser, which faithfully reproduces the main features of the observed microdisk laser mode as shown above.

4 Conclusions and Discussion

The formation of coherent polygon modes with ultrahigh Q factors has allowed for the realization of single-mode narrow-linewidth microlasers in single LN microdisks, which has significant implications for the miniaturization of optical systems in which highly coherent laser sources must be incorporated. To achieve a fully integrated EO tunable polygon mode microdisk laser, the suspended microdisk can be replaced with a microdisk sitting on the fused silica substrate to achieve better mechanical stability. A cladding layer of fused silica is then coated on the LNOI microdisk, which is flattened by polishing to support a coupling waveguide. Then, the fiber taper can be replaced with a waveguide lithographically fabricated on top of the fused silica cladding, and the polygon mode is formed by controlling the coupling location of the upper waveguide and lower LNOI microdisk, allowing for the construction of a fully integrated narrow-linewidth EO tunable polygon mode microdisk laser. Further exploration of the strong piezoelectric, acousto-optic, and second-order nonlinear properties of the LN will promote the performance and functionality of the single-mode microdisk laser in a straightforward manner without the necessity of heterogeneous integration.

Acknowledgments

T.L. and S.F. would like to acknowledge CMC Microsystems. The work was supported by the National Key R&D Program of China (2019YFA0705000), the National Natural Science Foundation of China (12192251, 62122079, 11734009, 62035013, 61635009, 62075192, 11874375, and 11874154), Shanghai Municipal Science and Technology Major Project (2019SHZDZX01), Science and Technology Commission of Shanghai Municipality (21DZ1101500), the Quantum Joint Funds of the Natural Foundation of Shandong Province (ZR2020LLZ007), the Fundamental Research Funds for the Central University, Nature Science and Engineering Research Council of Canada (NSERC) Discovery (RGPIN-2020-05938), and the Youth Innovation Promotion Association of Chinese Academy of Sciences (2020249). The authors declare no conflicts of interest related to this paper.

References

1. M. Kösters et al., "Optical cleaning of congruent lithium niobate crystals," *Nat. Photonics* **3**(9), 510–513 (2009).
2. Y. Kong et al., "Recent progress in lithium niobate: optical damage, defect simulation, and on-chip devices," *Adv. Mater.* **32**(3), 1806452 (2020).
3. A. Boes et al., "Status and potential of lithium niobate on insulator (LNOI) for photonic integrated circuits," *Laser Photonics Rev.* **12**(4), 1700256 (2018).
4. J. Lin et al., "Advances in on-chip photonic devices based on lithium niobate on insulator," *Photonics Res.* **8**(12), 1910–1936 (2020).
5. Y. Qi and Y. Li, "Integrated lithium niobate photonics," *Nanophotonics* **9**(6), 1287–1320 (2020).
6. Y. Jia, L. Wang, and F. Chen, "Ion-cut lithium niobate on insulator technology: recent advances and perspectives," *Appl. Phys. Rev.* **8**(1), 011307 (2021).
7. D. Zhu et al., "Integrated photonics on thin-film lithium niobate," *Adv. Opt. Photonics* **13**(2), 242–352 (2021).
8. M. Zhang et al., "Integrated lithium niobate electro-optic modulators: when performance meets scalability," *Optica* **8**(5), 652–667 (2021).
9. M. Xu et al., "High-performance coherent optical modulators based on thin-film lithium niobate platform," *Nat. Commun.* **11**(1), 3911 (2020).
10. C. Wang et al., "Monolithic lithium niobate photonic circuits for Kerr frequency comb generation and modulation," *Nat. Commun.* **10**(1), 978 (2019).
11. Y. He et al., "Self-starting bi-chromatic $LiNbO_3$ soliton microcomb," *Optica* **6**(9), 1138–1144 (2019).
12. Z. Gong et al., "Near-octave lithium niobate soliton microcomb," *Optica* **7**(10), 1275–1278 (2020).
13. J. Lin et al., "Broadband quasi-phase-matched harmonic generation in an on-chip monocrystalline lithium niobate microdisk resonator," *Phys. Rev. Lett.* **122**(17), 173903 (2019).
14. R. Luo et al., "Highly tunable efficient second-harmonic generation in a lithium niobate nanophotonic waveguide," *Optica* **5**(8), 1006–1011 (2018).
15. G.-T. Xue et al., "Ultrabright multiplexed energy-time-entangled photon generation from lithium niobate on insulator chip," *Phys. Rev. Appl.* **15**(6), 064059 (2021).
16. Y. Liu et al., "On-chip erbium-doped lithium niobate microcavity laser," *Sci. China Phys. Mech. Astron.* **64**(3), 234262 (2021).
17. Z. Wang et al., "On-chip tunable microdisk laser fabricated on Er^{3+}-doped lithium niobate on insulator," *Opt. Lett.* **46**(2), 380–383 (2021).
18. R. Gao et al., "On-chip ultra-narrow-linewidth single-mode microlaser on lithium niobate on insulator," *Opt. Lett.* **46**(13), 3131–3134 (2021).
19. Q. Luo et al., "On-chip erbium-doped lithium niobate microring lasers," *Opt. Lett.* **46**(13), 3275–3278 (2021).
20. T. Li et al., "A single-frequency single-resonator laser on erbium-doped lithium niobate on insulator," *APL Photonics* **6**(10), 101301 (2021).
21. R. Zhang et al., "Integrated lithium niobate single-mode lasers by the Vernier effect," *Sci. China Phys. Mech. Astron.* **64**(9), 294216 (2021).
22. Z. Xiao et al., "Single-frequency integrated laser on erbium-doped lithium niobate on insulator," *Opt. Lett.* **46**(17), 4128–4131 (2021).

23. T. Lu et al., "A narrow-linewidth on-chip toroid Raman laser," *IEEE J. Quantum Electron.* **47**(3), 320–326 (2011).
24. L. He et al., "Detecting single viruses and nanoparticles using whispering gallery microlasers," *Nat. Nanotechnol.* **6**(7), 428–432 (2011).
25. L. Feng et al., "Single-mode laser by parity-time symmetry breaking," *Science* **346**(6212), 972–975 (2014).
26. H. Rong et al., "A continuous-wave Raman silicon laser," *Nature* **433**(7027), 725–728 (2005).
27. T. Lu et al., "On-chip green silica upconversion microlaser," *Opt. Lett.* **34**(4), 482–484 (2009).
28. A. Schawlow and C. H. Townes, "Infrared and optical masers," *Phys. Rev.* **112**(6), 1940–1949 (1958).
29. C. H. Henry, "Theory of the linewidth of semiconductor lasers," *IEEE J. Quantum Electron.* **18**(2), 259–264 (1982).
30. P. Goldberg, P. W. Milonni, and B. Sundaram, "Theory of the fundamental laser linewidth," *Phys. Rev. A* **44**(3), 1969–1985 (1991).
31. K. J. Vahala, "Optical microcavities," *Nature* **424**(6950), 839–846 (2003).
32. Z. Fang et al., "Polygon coherent modes in a weakly perturbed whispering gallery microresonator for efficient second harmonic, optomechanical, and frequency comb generations," *Phys. Rev. Lett.* **125**(17), 173901 (2020).
33. R. Wu et al., "Lithium niobate microdisk resonators of quality factors above 107," *Opt. Lett.* **43**(17), 4116–4119 (2018).
34. D. Derickson, *Fiber Optic Test and Measurement*, Prentice Hall, Upper Saddle River, New Jersey (1998).
35. H. Jiang et al., "Fast response of photorefraction in lithium niobate microresonators," *Opt. Lett.* **42**(17), 3267–3270 (2017).
36. J. Wang et al., "Thermo-optic effects in on-chip lithium niobate microdisk resonators," *Opt. Express* **24**(19), 21869–21879 (2016).
37. T.-J. Wang et al., "On-chip optical microresonators with high electro-optic tuning efficiency," *J. Lightwave Technol.* **38**(7), 1851–1857 (2020).
38. A. Yariv and P. Yeh, *Photonics: Optical Electronics in Modern Communications*, 6th ed., Oxford University Press, New York (2007).
39. D. N. Nikogosyan, *Nonlinear Optical Crystals: A Complete Survey*, Springer, New York (2006).
40. X. Du, S. Vincent, and T. Lu, "Full-vectorial whispering-gallery-mode cavity analysis," *Opt. Express* **21**(19), 22012–22022 (2013).
41. X. Du et al., "Generalized full-vector multi-mode matching analysis of whispering gallery microcavities," *Opt. Express* **22**(11), 13507–13514 (2014).
42. A. Yariv, *Quantum Electronics*, 3rd ed., Wiley, New York (1991).

Jintian Lin is an associate professor at Shanghai Institute of Optics and Fine Mechanics, CAS. He received his BS degree in optical information science and technology from Sun Yat-sen University in 2009 and his PhD in optics from the University of Chinese Academy of Sciences in 2014. His current research interests include integrated optics, nonlinear optics, and micro/nano-processing.

Biographies of the other authors are not available.